



A non-destructive correlated energy spread monitor using multi-stripline electrodes for X-ray free electron lasers

Chang-Kyu Sung¹ · BokKyun Shin¹ · Moses Chung¹ · Inhyuk Nam² · Changbum Kim²

Received: 16 November 2022 / Accepted: 9 December 2022
© The Korean Physical Society 2023

Abstract

During X-ray free electron laser (XFEL) operation, electron beam parameters such as the correlated energy spread, which affects the self-amplified spontaneous emission (SASE) spectrum, should remain optimized for the best performance. However, the correlated energy spread often varies from the optimized condition owing to the drift of RF stations, even when a feedback system with low-level radio frequency is operating. Non-destructive correlated energy spread monitoring could offer a means to stabilize such variations and improve the performance of X-ray generation by maintaining the spectral quality. Herein, we investigated the feasibility of a non-destructive correlated energy spread monitor based on multi-stripline electrodes for use with the 200 pC electron beam at the Pohang Accelerator Laboratory XFEL (PAL-XFEL). Beam tracking and electromagnetic simulations indicated that the correlated energy spread up to approximately 0.1% could be measured without intercepting the beam at the bunch compressors of the PAL-XFEL. Through the 3D FEL simulation, we confirmed that keeping the SASE energy spectrum bandwidth to 0.05–0.15%, with a photon energy of 9.7 keV at the undulator, requires the correlated energy spread of the electron beam to be within 0.12–0.35% at the third bunch compressor. From the simulations, we conclude that the non-destructive correlated energy spread monitor based on multi-stripline electrodes is applicable to XFEL facilities and could serve as an effective optimization tool.

Keywords Free electron laser · Stripline beam position monitor · Correlated energy spread

1 Introduction

X-ray free electron lasers (XFELs) generate high-brightness coherent X-rays using high-current electron beams with ultrashort bunch lengths [1–5]. These facilities have enabled revolutionary experiments in many basic and applied sciences. The characterization of electron beam parameters, such as emittance, and uncorrelated and correlated energy spreads, is crucial for achieving the best performance in generating X-rays [6].

The uncorrelated energy spread is the RMS width of the phase-space ellipse along the energy axis after the

time-energy correlation (imprinted by the slope of the RF accelerating fields) is removed. The optimization of emittance and uncorrelated energy spread, which is mainly done in photocathode gun, can decrease the gain length, resulting in a shorter total undulator length for the saturation of the X-ray amplitude in normal self-amplified spontaneous emission (SASE) operation [7]. In contrast, by adjusting the RF phases of the linear accelerators, the correlated energy spread is optimized to produce a high spectral brightness from a narrow SASE spectrum. With the optimum correlated energy spread, the high-peak-current electron beam produced by reducing the bunch length through a magnetic chicane bunch compressor compensates for the loss of beam energy driven by the wakefields along the long undulator. Thus, the best X-ray performance, determined by the spectral brightness and bandwidth, can be achieved by optimizing those electron beam parameters.

The correlated energy spread is usually determined from the measured horizontal beam distribution by the screen monitor inserted in the bunch compressor. Whereas the accuracy of this destructive method is quite satisfactory, it

✉ Moses Chung
mchung@unist.ac.kr

Inhyuk Nam
ihnam@postech.ac.kr

¹ Department of Physics, Ulsan National Institute of Science and Technology, Ulsan 44919, Korea

² Pohang Accelerator Laboratory, Pohang 37673, Korea

cannot be used for a real-time feedback system to the correlated energy spread because it stops the beam propagation.

During the actual operation, however, the correlated energy spread can vary from the optimized condition because the RF station of the accelerating columns drifts, even though a feedback system for the low-level radio frequency (LLRF) is in operation. To control the correlated energy spread, the phase and amplitude of the RF station for the accelerating columns must be adjusted appropriately. With real-time monitoring of the correlated energy spread in a non-destructive manner, the RF station could be operated to maintain the correlated energy spread at the optimum condition.

In 2003, Suwada et al. experimentally demonstrated the non-destructive measurement of energy spread for the high-charge electron beams (0.9 nC/bunch and 8 nC/bunch) by implementing a multi-stripline monitor at the dispersive section [8, 9]. In the case of XFEL, the magnetic chicane bunch compressor forms the dispersive section in the linear accelerator. This suggests that non-destructive monitoring based on the multi-stripline could be applicable to XFEL facilities.

Herein, we investigated the feasibility of non-destructive correlated energy spread monitoring for the low-charge electron beam (200 pC/bunch) of the XFEL system at the Pohang Accelerator Laboratory (PAL-XFEL). We performed beam tracking simulations using the ELEGANT code [10] to check the electron beam parameters at the bunch compressors of the PAL-XFEL, and estimated the expected range of the correlated energy spread at each bunch compressor. In addition, we performed an electromagnetic simulation using the CST program [11] and optimized the multi-stripline structure following the design in [12, 13]. Then, we performed a 3D FEL simulation and compared the spectral density of X-rays depending on the correlated energy spread of the electron beam.

In Sect. 2, we explain the principle of non-destructive monitoring for the energy spread of the beam, which is based on the multipole moment expansion of the beam-induced electromagnetic field, depending on the beam distribution. The beam distribution is affected by the energy spread at the dispersive section and yields the second-order (quadrupole and/or skew) moments of the electromagnetic field. At the XFEL facility, beam distribution deformation due to the energy spread occurs at a bunch compressor, which consists of four dipole magnets. We describe the relationship between the correlated energy spread of the electron beam and the quadrupole moment of the distribution in Sect. 3 by using a transfer matrix. Section 4 illustrates the signal responses of the stripline to the quadrupole moment obtained through the electromagnetic simulation, and compares the signal characteristics of a flat beam with those of a round beam with a symmetric beam cross-section. In Sect. 5, we discuss the application

of the non-destructive correlated energy spread monitoring to the electron beam of the PAL-XFEL. We estimated the quadrupole moment of the beam by varying the correlated energy spread at the bunch compressor, and investigated its effects on the SASE spectrum at a photon energy of 9.7 keV.

2 Multipole moment analysis of a charged particle beam distribution

A charged particle traveling through a conducting vacuum chamber generates an electromagnetic field; thus, an image current is induced on the inner surface of the surrounding chamber due to the electromagnetic field. The formula for the image current induced on the inner surface of a cylindrical chamber can be obtained by solving the electrostatic potential problem in the case of a relativistic beam [14] as derived in [15–17]. Once a particle moves parallel to the z -axis at a position (ρ, ϕ) in the transverse plane, it induces a surface image current density at the chamber wall, which is expressed as [15]

$$k(\rho, \phi, r, \theta) = \frac{i}{2\pi r} \frac{r^2 - \rho^2}{r^2 + \rho^2 - 2r\rho \cos(\phi - \theta)}. \quad (1)$$

Equation (1) describes the surface current density k induced by a single-line current i at a transverse position (ρ, ϕ) over an arbitrary point (r, θ) on the surface of the chamber. When the particle moves along the longitudinal axis in the beam-line, ρ is very small compared to the radius of the surrounding chamber r , such that $\rho/r \ll 1$. This ensures that Eq. (1) can be expanded in terms of ρ/r as follows [16]:

$$k(\rho, \phi, r, \theta) = \frac{i}{2\pi r} \left[1 + 2 \sum_{n=1}^{\infty} \left(\frac{\rho}{r} \right)^n \cos\{n(\phi - \theta)\} \right]. \quad (2)$$

For practical use, Eq. (2) must be changed into a function of the beam distribution parameters rather than single particle quantities. To find an expression for the density of the surface image current attributed to the transverse beam distribution, we replace the current delivered from a single line i with the current density distribution $J(\rho, \phi)$ as in [8], where $I_{\text{beam}} = \int J(\rho, \phi) \rho d\rho d\phi$ denotes the total beam current. By integrating Eq. (2) with the distribution function over the region occupied by the beam (ρ and ϕ), we obtain the density of the surface image current attributed to the beam as

$$K(r, \theta) = \frac{I_{\text{beam}}}{2\pi r} \times \left[1 + \frac{2\rho_0}{r} \cos(\theta - \phi_0) + \frac{2\rho_0^2}{r^2} \cos 2(\theta - \phi_0) + 2 \frac{\sigma_x^2 - \sigma_y^2}{r^2} \cos 2(\theta + \phi_{\text{skew}}) + \mathcal{O}(\rho, \phi) \right], \quad (3)$$

where ρ_0 is the dipole moment and describes the centroid of the beam with a polar coordinate ϕ_0 , ϕ_{skew} denotes the skew angle when the beam is rotated in the transverse plane, and σ_x (σ_y) is the RMS beam size along the horizontal (vertical) axis (see Fig. 1).

The difference in the squares of the RMS beam sizes ($\sigma_x^2 - \sigma_y^2$) defines the quadrupole moment of the beam. The last term $\mathcal{O}(\rho, \phi)$ on the right hand side of Eq. (3) represents the higher-order moments for $n \geq 3$, which are assumed to be negligible. As shown in Eq. (3), depending on the moments of the beam distribution, the current signal induced in the multi-stripline electrodes is represented as a periodic function of the polar angle θ . To find the moments of the beam distribution, we fit the current signal data to an equation composed as a sum of cosine functions as in Eq. (4), and then obtain the parameters in Eq. (3).

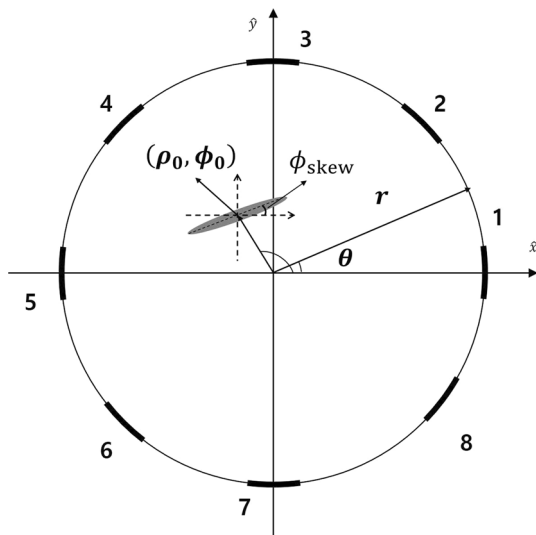


Fig. 1 Schematic diagram illustrating the beam cross-section and eight-stripline electrodes around the vacuum chamber. We assume that both the electrode and chamber surfaces are located at the radius r . In Ref. [8], the eight striplines were tilted by 22.5° with respect to the configuration here, to prevent any synchrotron radiation and off-energy electrons from impinging on the electrode surfaces. In our application, the expected charge is much lower; thus, we chose the present configuration to increase the signal sensitivity

$$F = A_0 + A_1 \cos(\theta - B_1) + (A_1^2/2A_0) \cos 2(\theta - B_1) + A_2 \cos 2(\theta - B_2). \quad (4)$$

It can be seen that the fitting parameter A_2 is directly related with the quadrupole moment in Eq. (3). Further details on Eqs. (3) and (4) can be found in Appendix A.

In this study, we consider implementing eight-stripline electrodes for reconstruction of the quadrupole moment of the beam at the bunch compressor, which could provide valuable information on the correlated energy spread of the XFEL facility. The detailed relationship between the quadrupole moment and the correlated energy spread at the bunch compressor is presented in the next section.

3 Quadrupole beam moment and correlated energy spread at bunch compressor

In this section, we derive a mathematical expression for the quadrupole beam moment in a magnetic-chicane bunch compressor by using a transfer matrix R . The transfer matrix maps the beam coordinates from the entrance of the bunch compressor to the measurement position in the dispersive section. We consider the horizontal plane to be the bending plane for the bunch compressor, which consists of four dipole magnets. The position coordinates at the measurement point in the bunch compressor can then be obtained in terms of the matrix elements R_{ij} as

$$x = R_{11}x_0 + R_{12}x'_0 + R_{16} \frac{\Delta E}{E_0}, \quad (5)$$

$$y = R_{33}y_0 + R_{34}y'_0, \quad (6)$$

where x_0 and x'_0 (y_0 and y'_0) are the horizontal (vertical) positions and divergences, respectively, at the entrance of the bunch compressor, and $\Delta E/E_0$ is the fractional energy deviation. Detailed expressions for the matrix elements R_{ij} can be found in Appendix B.

The quadrupole moment ($\sigma_x^2 - \sigma_y^2$) is expressed as

$$\sigma_x^2 - \sigma_y^2 = R_{16}^2 \langle (\Delta E/E_0)^2 \rangle + \epsilon_{x0} (\beta_{x0} R_{11}^2 + \gamma_{x0} R_{12}^2 - 2R_{11}R_{12}\alpha_{x0}) - \epsilon_{y0} (\beta_{y0} R_{33}^2 + \gamma_{y0} R_{34}^2 - 2R_{33}R_{34}\alpha_{y0}), \quad (7)$$

where $(\alpha_{x0}, \beta_{x0}, \gamma_{x0})$ and $(\alpha_{y0}, \beta_{y0}, \gamma_{y0})$ are the horizontal and vertical Twiss parameters, respectively, and ϵ_{x0} and ϵ_{y0} are the horizontal and vertical RMS emittances at the entrance of the bunch compressor, respectively. Here, $\langle (\Delta E/E_0)^2 \rangle$ denotes the square of the correlated energy spread averaged over the beam distribution. Because $\sigma_E \equiv \sqrt{\langle (\Delta E/E_0)^2 \rangle}$, we rewrite Eq. (7) for σ_E as a function of $(\sigma_x^2 - \sigma_y^2)$:

$$\sigma_E^2 = \frac{1}{R_{16}^2} \times \left[(\sigma_x^2 - \sigma_y^2) - \epsilon_{x0} (\beta_{x0} R_{11}^2 + \gamma_{x0} R_{12}^2 - 2R_{11} R_{12} \alpha_{x0}) + \epsilon_{y0} (\beta_{y0} R_{33}^2 + \gamma_{y0} R_{34}^2 - 2R_{33} R_{34} \alpha_{y0}) \right]. \quad (8)$$

Therefore, substituting the well-characterized emittances and Twiss parameters at the entrance of the bunch compressor into Eq. (8), the quadrupole moment reconstructed in the bunch compressor can provide the correlated energy spread of the electron beam.

4 Signal responses of striplines to quadrupole beam moment

In this section, we present an estimation of the signal responses of the striplines to the quadrupole moment of the beam by performing electromagnetic simulations using the CST software package [11]. We optimized the structure of the striplines using the dimensions listed in Table 1, following the design concepts given in [12, 13]. Then, we generated a Gaussian electron beam with a charge of 200 pC and bunch length of 10 mm in the simulation, and transported it through the structure illustrated in Fig. 2. To conveniently change the values of the quadrupole moment, we loaded two particle sources separated by a distance that was directly related to the quadrupole moment (see Fig. 2). We then estimated how the eight-stripline beam position monitor (BPM) responds to the quadrupole moment of the beam, and determined the signal difference between the cases of the elongated ($\sigma_x^2 > \sigma_y^2$) and round ($\sigma_x^2 = \sigma_y^2$) beams.

In the simulation, we ensured that the beam centroid remained at the center of the chamber. In this way, we excluded any contribution from the dipole moment ρ_0 , as shown in Eq. (3).

Considering this, we first estimated the response of the stripline to a single round beam, which is simply a single particle source at the center with $\sigma_x^2 = \sigma_y^2$ and vanishing quadrupole moment.

Table 1 Design parameters of the eight-stripline beam position monitor. The stripline design was optimized following Ref. [12]

Parameter	Value
Outer radius (mm)	22
Inner radius (mm)	19
Opening angle (°)	23
Electrode thickness (mm)	1
Electrode length (mm)	120

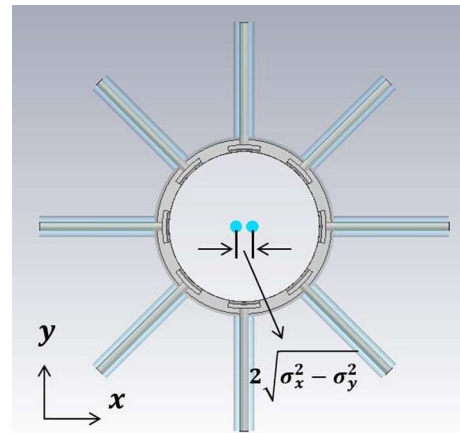


Fig. 2 In the CST simulation, a beam composed of two particle sources was generated around the center of stripline structure. These sources were separated by a distance that is directly related to the quadrupole moment

Compared with this result, we then evaluated how the signal response would change when a quadrupole moment was induced.

A parameter condition, $\rho_0 = \phi_0 = \phi_{\text{skew}} = 0$, was set in the simulation. The quadrupole moment was varied from 0.01 to 0.25 mm^2 by changing the distance between the two particle sources, and the voltage signal of the stripline was estimated. The range of quadrupole moments used in the simulation covered the lower limits of the quadrupole moments expected at the bunch compressors of the PAL-XFEL, which are discussed in the next section.

Figure 3 shows the simulation results for electron beams of 50 pC and 200 pC bunch charges and 10 mm Gaussian bunch length. Here, V_Q and V_R represent the amplitudes in

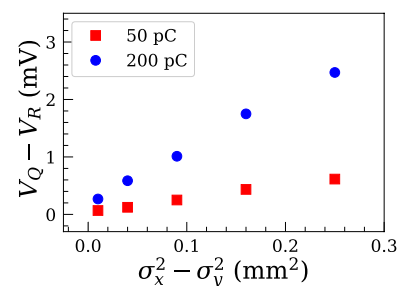


Fig. 3 The voltage signal response of the stripline contributed by the quadrupole moment of the beam distribution. In this case, a stripline was placed along the positive x -axis. Here, V_Q and V_R represent the stripline responses in the voltage signal to the elongated beam with a finite quadrupole moment and to the round beam, respectively. The difference of ($V_Q - V_R$) is approximately linearly proportional to the quadrupole moment when $\rho_0 = \phi_0 = \phi_{\text{skew}} = 0$. Based on the simulation, we estimate that the bunch charge of 50 pC and quadrupole moment of 0.01 mm^2 are the lowest levels in which the proposed method would work

the voltage signal to the elongated beam with a finite quadrupole moment and to the round beam, respectively.

The signal was detected by a stripline placed exactly on the positive x -axis as shown in Fig. 2. Hence, when the beam is elongated, the quadrupole moment increases and the signal amplitude of this stripline is affected most strongly. Following Eq. (3) in Sect. 2, we can see that the difference of ($V_Q - V_R$) shown in Fig. 3 is approximately linearly proportional to the quadrupole moment when $\rho_0 = \phi_0 = \phi_{skew} = 0$.

This result indicates that the quadrupole moment of the beam causes the difference in the voltage amplitude with respect to the round-beam case. For example, voltage amplitudes of $70 \mu\text{V}$ (50 pC/bunch) and $200 \mu\text{V}$ (200 pC/bunch) were obtained when the quadrupole moment was 0.01 mm^2 .

Taking the noise signal of $\sim 10 \mu\text{V}$ due to the RF system into account, such signal differences can be considered as lower limits for distinguishing the quadrupole moment of a beam distribution with the MicroTCA-based electronics used in the PAL-XFEL [18, 19].

According to [20], however, the beam distribution can be tilted in the transverse plane at the bunch compressor so that we have $\phi_{skew} \neq 0$. In such a case, the signal difference attributed by the elongated beam with a finite quadrupole moment is seen at the stripline placed along a diagonal axis. In other words, for the general case, the quadrupole moment of the beam distribution needs to be measured along with the

skew angle ϕ_{skew} , and this can be achieved with the proposed multi-stripline BPM.

As for a preliminary experiment, we fabricated the multi-stripline BPM and installed it in the RF photo-injector test facility of the PAL as shown in Fig. 4a. The BPM was located at the downstream of the dipole magnet and the screen monitor with a material of YAG:Ce was following by a distance of 0.25 m. We produced a 70 pC electron beam with the photocathode and accelerated it to 4 MeV through the S-band cavity (2.856 GHz) at the gun. We then varied the quadrupole moment at the multi-stripline by changing the RF phase of the gun cavity. We measured the variation of quadrupole moment by means of the multi-stripline BPM and screen monitor. Figure 4b shows the preliminary results for the 70 pC electron beam. By comparing the measurement results from both systems, we confirmed the feasibility of the multi-stripline BPM for measuring the quadrupole moment.

5 Application to electron beam of PAL-XFEL

The PAL-XFEL consists of three bunch compressors, as shown in Fig. 5. Figure 5 also describes the diagnostic system and the measured transverse beam profiles, which are stretched along the horizontal direction owing to the correlated energy spread at the bunch compressor. The

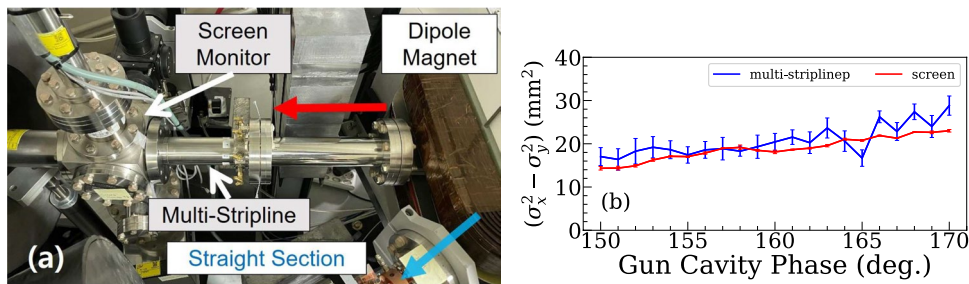


Fig. 4 Preliminary experimental setup (a) and measurement results (b). The multi-stripline was installed behind the dipole magnet and followed by the screen monitor. Electron beams (red arrow) of 4 MeV

and 70 pC were used in this test. The standard errors for the multi-stripline measurements are approximately 7%

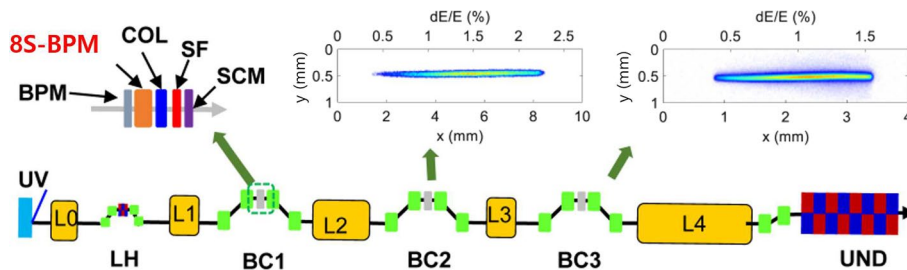


Fig. 5 Schematic of the PAL-XFEL. The insets are measured dispersive beam profiles at the center of the bunch compressors. BPM: beam position monitor, 8S-BPM: eight-stripline BPM, COL: colli-

imator, SF: slotted foil, SCM: screen monitor, LH: laser heater, BC: bunch compressor, UND: undulator, L0-4: accelerating section

bunch compressors are operated with the parameters listed in Table 2 [21], which also summarizes the electron beam parameters at each bunch compressor entrance, including the correlated energy spread σ_E .

With the parameters in Table 2, we performed tracking simulations using the ELEGANT code [10] to calculate the quadrupole moments with varying correlated energy spread. We generated an electron beam of 200 pC with the Twiss parameters, as listed in Table 2, and transported it through the bunch compressor. Then, we estimated the quadrupole moment in the bunch compressor by varying the correlated energy spread σ_E at the entrance of the bunch compressor from the typical values specified in Table 2. We kept the emittance and Twiss parameters unchanged. Although those parameters could have a bunch-to-bunch fluctuation of about $\pm 10\%$, such jitters contribute negligibly small to the quadrupole moment. That is, the correlated energy spread is directly related to the quadrupole moment at the bunch compressor.

The simulation results are shown in Fig. 6 for each bunch compressor. Figure 6 shows that the quadrupole moment is greater than approximately 0.05 mm^2 which is expected at the bunch compressor 3. This lower limit of the quadrupole moment was obtained with a correlated energy spread of $\sim 0.1\%$. According to Fig. 3, the quadrupole moment of 0.05 mm^2 induces a voltage signal difference of approximately 1 mV compared to the round beam. We anticipate that the degree of the quadrupole moment at the bunch compressors of the PAL-XFEL would create a sufficient signal intensity to monitor the correlated energy spread of an electron beam using the stripline.

At the PAL-XFEL, during normal operation based on the SASE process, the typical spectral bandwidth of the X-ray pulse is approximately 0.1%. However, this bandwidth can vary because the phase and amplitude of an RF station drift depending on environmental conditions, even when the LLRF feedback system is applied. The drift in the RF system changes the correlated energy spread at the undulator, thus affecting the SASE bandwidth of the X-ray pulses. Therefore, when non-destructive energy spread monitoring at the bunch compressor is possible, we could estimate the

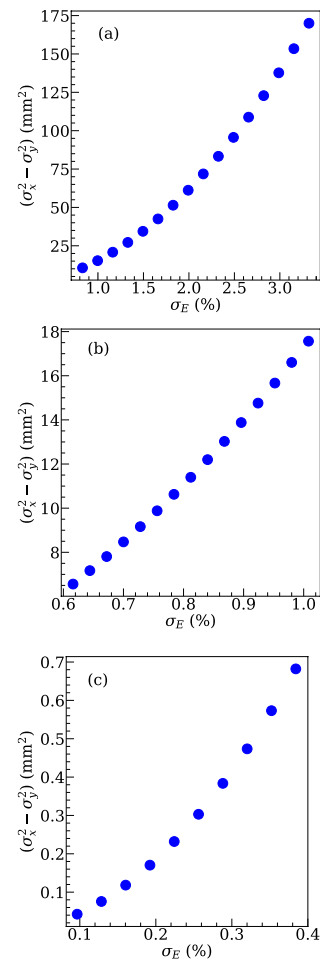


Fig. 6 Quadrupole moments evaluated between the second and third bending magnets as a function of the correlated energy spread at a bunch compressor 1, **b** bunch compressor 2 and **c** bunch compressor 3

correlated energy spread of an electron beam at the undulator as well, which will be useful for improving the online SASE bandwidth.

We simulated three cases of electron beams with different energy spreads at the bunch compressor 3 (0.12, 0.25, and 0.35%), as listed in Table 3. Accordingly, the quadrupole moments at the third bunch compressor and the correlated

Table 2 Electron beam parameters at each bunch compressor. $\epsilon_{nx,ny}$: normalized horizontal and vertical emittance, $\alpha_x, \alpha_y, \beta_x, \beta_y$: Twiss parameters at the entrance, E_0 : mean energy, σ_E : RMS correlated energy spread, D_x : dispersion function for each bunch compressor, θ : bending angle of a dipole magnet, R_{56} : bunch compressor parameter

	Bunch compressor 1	Bunch compressor 2	Bunch compressor 3
$\epsilon_{nx}/\epsilon_{ny}$ ($\mu\text{m}/\mu\text{m}$)	0.5/0.5	0.5/0.5	0.5/0.5
α_x/α_y	2.54/1.04	2.48/0.15	2.67/−0.09
β_x/β_y (m/m)	28.3/4.20	39.5/6.96	47.8/11.9
E_0 (GeV)	0.35	2.5	3.4
σ_E (%)	2.3	0.8	0.25
D_x (m)	−0.4	−0.35	−0.22
θ (°)	4.97	3.0	1.6
R_{56} (mm)	−66.7	−36.7	−11.6

Table 3 Correlated energy spreads and the corresponding transverse beam parameters at bunch compressor 3 (BC3) and the undulator (UND)

	Case 1	Case 2	Case 3
σ_x/σ_y at BC3 (mm)	0.28/0.04	0.55/0.04	0.76/0.04
$\sigma_x^2 - \sigma_y^2$ at BC3 (mm ²)	0.08	0.30	0.57
Energy spread at BC3 (%)	0.12	0.25	0.35
Energy spread at UND (%)	0.05	0.10	0.15
Beam energy at BC3 (GeV)	3.5	3.5	3.5
Beam energy at UND (GeV)	8.5	8.5	8.5

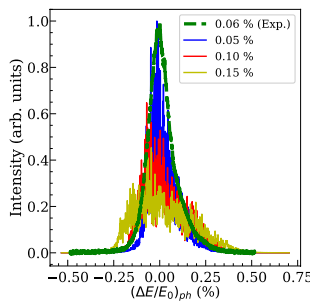


Fig. 7 SASE FEL spectra with different correlated beam energy spreads at the central photon energy of 9.7 keV; simulations: 0.05, 0.1, and 0.15% (solid lines), experiment: 0.06% (dashed line). The parameters in Table 3 are used for the 3D FEL simulations. Here, the simulation results are shown after averaging over ten shots, while the experimentally measured data was averaged over 100 shots. In the experiment, the intrinsic shot-to-shot fluctuations of intensity and spectral bandwidth are normally in the range from 10 to 20%. The wakefield effects in the undulator are also included in the 3D FEL simulations

energy spread at the undulator were calculated. In Sect. 4, we confirmed that these quadrupole moment levels can be measured using the proposed eight-stripline BPM system. We performed 3D FEL simulations to observe the effects in the SASE spectrum according to the three cases of correlated energy spread at the undulator (0.05, 0.10, and 0.15%), with a central photon energy of 9.7 keV. A beam energy of 8.54 GeV, an uncorrelated energy spread of 1.5×10^{-4} , a beam charge of 180 pC, and a peak current of 3 kA were used for the simulations. Figure 7 shows the simulated spectra of hard X-ray pulses for different cases of the correlated energy spread at the undulator (solid lines), along with the experimental data for 0.06% energy spread case (dashed line).

Considering approximately 10–20% of error bar, we note that the measured spectrum with 0.06% case lies approximately in between the 0.05 and 0.10% simulation cases. The 0.05% energy spread case results in a spectral intensity almost three times higher than that in the 0.15% case. To keep the spectral intensity optimized during operation, the correlated

energy spread should be corrected before the undulator. Therefore, the proposed non-destructive energy spread monitor can be an effective tool for providing the best X-ray pulse quality by correcting the energy spread at the undulator.

6 Conclusion

In this paper, we proposed a non-destructive correlated energy spread monitoring system based on a multi-stripline BPM, and numerically investigated its feasibility for use in XFEL facilities. With the tracking simulation for the electron beam of the PAL-XFEL, the quadrupole moment was numerically estimated to be greater than 0.05 mm^2 at the bunch compressor when the correlated energy spread varied by approximately $\pm 0.1\%$ from the normal operation.

According to the electromagnetic simulation, the stripline responds to the quadrupole moment of 0.05 mm^2 for the 200 pC electron beam by about 1 mV in the voltage difference. Hence, while measuring the correlated energy spread of the electron beam at the bunch compressor 3 would be rather challenging, we expect that it is feasible at least at the bunch compressors 1 and 2 using modern MicroTCA-based electronics [22]. Indeed, the experimental results in Fig. 4b demonstrate that our measurement system covers the quadrupole moment ranges expected for the first and second bunch compressors. The 3D FEL simulation shows that non-destructive correlated energy spread monitoring offers the possibility to enhance the quality of X-ray generation by maintaining optimized condition for the electron beam parameters. In conclusion, we believe that this type of non-destructive correlated energy spread monitor is applicable to the electron beams of modern XFEL facilities, and can serve as a unique tool for controlling the X-ray spectrum.

Acknowledgements This work was supported by the National Research Foundation (NRF) of Korea (Grant No. NRF-2020R1A2C1010835, No. NRF-2016R1A5A1013277 and NRF-2022R1A2C2009768), and also by the Pohang Accelerator Laboratory.

Appendix A: Surface image current density induced by a two dimensional Gaussian beam distribution

We have the series representation of Eq. (2) as

$$k(\rho, \phi, r, \theta) = \frac{i}{2\pi r} \times \left[1 + \frac{2}{r}(x \cos \theta + y \sin \theta) + \frac{2}{r^2} \{ (x^2 - y^2) \cos 2\theta + 2xy \sin 2\theta \} + \mathcal{O}(\rho, \phi) \right], \quad (\text{A1})$$

with $x = \rho \cos \phi$ and $y = \rho \sin \phi$. After replacing the single-line current i with the beam current density distribution J , we obtain

$$K(x, y, r, \theta) = \int \int dx dy \left[1 + \frac{2}{r}(x \cos \theta + y \sin \theta) + \frac{2}{r^2} \{ (x^2 - y^2) \cos 2\theta + 2xy \sin 2\theta \} + \mathcal{O}(\rho, \phi) \right] \frac{J(x, y)}{2\pi r}. \tag{A2}$$

Now, we assume that the beam current density distribution is a two-dimensional Gaussian function in the following form:

$$J(x, y) = \frac{I_{\text{beam}}}{2\pi\sigma_x\sigma_y} \times \exp \left[-a(x - x_0)^2 - 2b(x - x_0)(y - y_0) - c(y - y_0)^2 \right], \tag{A3}$$

where the constants a , b , and c are given by

$$a = \frac{\cos^2 \phi_{\text{skew}}}{2\sigma_x^2} + \frac{\sin^2 \phi_{\text{skew}}}{2\sigma_y^2},$$

$$b = -\frac{\sin 2\phi_{\text{skew}}}{4\sigma_x^2} + \frac{\sin 2\phi_{\text{skew}}}{4\sigma_y^2},$$

$$c = \frac{\sin^2 \phi_{\text{skew}}}{2\sigma_x^2} + \frac{\cos^2 \phi_{\text{skew}}}{2\sigma_y^2}.$$

Here, ϕ_{skew} is the tilt angle of the beam in the transverse plane, and (x_0, y_0) denotes the beam centroid. Substituting Eq. (A3) into Eq. (A2) and performing the double integral give

$$K(r, \theta) = \frac{I_{\text{beam}}}{2\pi r} \times \left[1 + \frac{2\rho_0}{r} \cos(\theta - \phi_0) + \frac{2\rho_0^2}{r^2} \cos 2(\theta - \phi_0) + 2 \frac{\sigma_x^2 - \sigma_y^2}{r^2} \cos 2(\theta + \phi_{\text{skew}}) + \mathcal{O}(\rho, \phi) \right]. \tag{A4}$$

Here, $x_0 = \rho_0 \cos \phi_0$ and $y_0 = \rho_0 \sin \phi_0$. By introducing a calibration factor C , we can define the following fitting parameters for the voltage signal response of the stripline in Eq. (4):

$$A_0 = C \frac{I_{\text{beam}}}{2\pi r}, \tag{A5}$$

$$A_1 = A_0 \frac{2\rho_0}{r}, \tag{A6}$$

$$A_2 = A_0 2 \frac{\sigma_x^2 - \sigma_y^2}{r^2}. \tag{A7}$$

We note that the fitting errors in A_0 and A_2 are propagated into the determination of $(\sigma_x^2 - \sigma_y^2)$.

Appendix B: Transfer matrix for bunch compressor

The bunch compressor consists of four dipole magnets with bending radius and angle ρ and θ , respectively, with an arc length of $L_B = \rho\theta$. The first and second (third and fourth) magnets are separated by the distance of d , and the third follows the second by the distance ℓ as illustrated in Fig. 8.

Each magnet is treated as a combination of the sector and wedge magnets, with the matrix representations given in Eqs. (B1) and (B2), respectively, where the horizontal plane is the bending plane.

$$M_{\text{sector}} = \begin{bmatrix} \cos \theta & \rho \sin \theta & 0 & 0 & 0 & \rho(1 - \cos \theta) \\ -\frac{\sin \theta}{\rho} & \cos \theta & 0 & 0 & 0 & \sin \theta \\ 0 & 0 & 1 & \rho\theta & 0 & 0 \\ 0 & 0 & 0 & 1 & 0 & 0 \\ \sin \theta & \rho(1 - \cos \theta) & 0 & 0 & 1 & -\rho(\theta - \sin \theta) \\ 0 & 0 & 0 & 0 & 0 & 1 \end{bmatrix}, \tag{B1}$$

and

$$M_{\text{wedge}} = \begin{bmatrix} 1 & 0 & 0 & 0 & 0 & 0 \\ \frac{\tan \theta}{\rho} & 1 & 0 & 0 & 0 & 0 \\ 0 & 0 & 1 & 0 & 0 & 0 \\ 0 & 0 & -\frac{\tan \theta}{\rho} & 1 & 0 & 0 \\ 0 & 0 & 0 & 0 & 1 & 0 \\ 0 & 0 & 0 & 0 & 0 & 1 \end{bmatrix}. \tag{B2}$$

The transfer matrix for any position in the bunch compressor can then be determined by matrix multiplications. For the multi-stripline position (assuming that the multi-stripline BPM is located just in front of the third bending magnet to maximize the signal sensitivity), the corresponding transfer matrix is determined as follows:

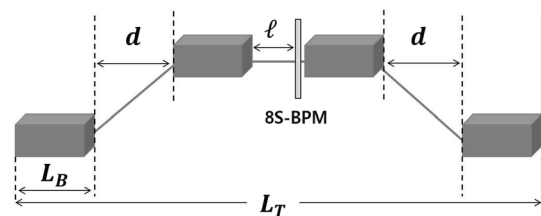


Fig. 8 Schematic diagram of a bunch compressor

$$M = M_D(\ell) \cdot M_{\text{sector}}(-\rho, -\theta) \cdot M_{\text{wedge}}(-\rho, -\theta) \cdot M_D(d) \cdot M_{\text{wedge}}(\rho, \theta) \cdot M_{\text{sector}}(\rho, \theta), \quad (B3)$$

where M_D denotes the transfer matrix of the drift space.

By evaluating Eq. (B3), we obtain a matrix in the form

$$M_B = \begin{bmatrix} R_{11} & R_{12} & 0 & 0 & R_{15} & R_{16} \\ R_{21} & R_{22} & 0 & 0 & R_{25} & R_{26} \\ 0 & 0 & R_{33} & R_{34} & 0 & 0 \\ 0 & 0 & R_{43} & R_{44} & 0 & 0 \\ R_{51} & R_{52} & 0 & 0 & R_{55} & R_{56} \\ R_{61} & R_{62} & 0 & 0 & R_{65} & R_{66} \end{bmatrix}, \quad (B4)$$

where the explicit expressions for each element are given as

$$\begin{aligned} R_{11} &= R_{22} = R_{55} = R_{66} = 1, \\ R_{15} &= R_{21} = R_{25} = R_{26} = R_{51} = R_{61} = R_{62} = R_{65} = 0, \\ R_{12} &= \ell + 2\rho \tan \theta + \frac{d}{\cos^2 \theta}, \\ R_{16} &= \frac{1}{\cos \theta} (2\rho - 2\rho \cos \theta + d \tan \theta), \\ R_{33} &= 1 - 2\theta \tan \theta - \frac{(d + 2\ell) \tan \theta}{\rho} \frac{d(\ell + \rho\theta) \tan^2 \theta}{\rho^2}, \\ R_{34} &= (d + \ell + 2\rho\theta) - 2(d + \ell + \rho\theta)\theta \tan \theta \\ &\quad - \frac{d\ell \tan \theta}{\rho} + (\ell + \rho\theta) \frac{d\theta \tan^2 \theta}{\rho}, \\ R_{43} &= -\frac{2 \tan \theta}{\rho} + \frac{d \tan^2 \theta}{\rho^2}, \\ R_{44} &= 1 - 2\theta \tan \theta - \frac{d(1 - \theta \tan \theta) \tan \theta}{\rho}, \\ R_{52} &= \frac{1}{\cos \theta} (2\rho - 2\rho \cos \theta + d \tan \theta), \\ R_{56} &= -2\rho\theta + 2\rho \tan \theta + d \tan^2 \theta. \end{aligned}$$

By substituting these expressions into Eq. (7) in Sect. 3, we obtain an explicit relation between the quadrupole moment and the correlated energy spread of an electron beam at the bunch compressor. Therefore, using the well-characterized RMS emittances and Twiss parameters, the reconstruction of the quadrupole moment provides the correlated energy spread of an electron beam at the XFEL facility.

References

1. P. Emma, R. Akre, J. Arthur et al., First lasing and operation of an ångstrom-wavelength free-electron laser. *Nat. Photonics*, **4**, 641–647 (2010). <https://doi.org/10.1038/nphoton.2010.176>
2. E. Allaria, D. Castronovo, P. Cinquegrana et al., Two-stage seeded soft X-ray free-electron laser. *Nat. Photonics*, **7**, 913–918 (2013). <https://doi.org/10.1038/nphoton.2013.277>
3. H.-S. Kang, C.-K. Min, H. Heo et al., Hard X-ray free-electron laser with femtosecond-scale timing jitter. *Nat. Photonics*, **11**, 708–713 (2017). <https://doi.org/10.1038/s41566-017-0029-8>
4. W. Decking, S. Abeghyan, P. Abramian et al., A MHz-repetition-rate hard X-ray free-electron laser driven by a superconducting linear accelerator. *Nat. Photonics*, **14**, 391–397 (2020). <https://doi.org/10.1038/s41566-020-0607-z>
5. E. Prat, R. Abela, M. Aiba et al., A compact and cost-effective hard X-ray free-electron laser driven by a high-brightness and low-energy electron. *Nat. Photonics*, **14**, 748–754 (2020). <https://doi.org/10.1038/s41566-020-00712-8>
6. Z. Huang, K.-J. Kim, Review of x-ray free-electron laser theory. *Phys. Rev. ST Accel. Beams* **10**, 034801 (2007). <https://doi.org/10.1103/PhysRevSTAB.10.034801>
7. Y. Chen, I. Zagorodnov, M. Dohlus, Beam dynamics of realistic bunches at the injector section of the european x-ray free-electron laser. *Phys. Rev. Accel. Beams* **23**, 044201 (2020). <https://doi.org/10.1103/PhysRevAccelBeams.23.044201>
8. T. Suwada, M. Satoh, K. Furukawa, Nondestructive beam energy-spread monitor using multi-strip-line electrodes. *Phys. Rev. ST Accel. Beams* **6**, 032801 (2003). <https://doi.org/10.1103/PhysRevSTAB.6.032801>
9. T. Suwada, M. Satoh, K. Furukawa, New energy-spread-feedback control system using nondestructive energy-spread monitors. *Phys. Rev. ST Accel. Beams* **8**, 112802 (2005). <https://doi.org/10.1103/PhysRevSTAB.8.112802>
10. M. Borland, Elegant: A flexible sdds-compliant code for accelerator simulation, Tech. Rep. LS-287, Argonne National Lab., IL (US) (2000). <https://doi.org/10.2172/761286>
11. www.cst.com
12. C. Kim, S. Lee, J. Hong et al., Stripline beam position monitor for X-ray free electron laser of pohang accelerator laboratory. *Rev. Sci. Instrum.* **90**, 093306 (2019). <https://doi.org/10.1063/1.5109421>
13. P. Forck, Beam instrumentation and diagnostics, arXiv preprint [arXiv:2009.10411](https://arxiv.org/abs/2009.10411) (2020). <https://doi.org/10.48550/arXiv.2009.10411>
14. J.D. Jackson, *Classical electrodynamics*, 3rd edn. (John Wiley & Sons, Inc., 1999)
15. R.E. Shafer, Beam position monitoring in AIP conference proceedings **249**, 601–636 (1992). <https://doi.org/10.1063/1.41980>
16. R. H. Miller et al., Nonintercepting emittance monitor, Tech. Rep. SLAC-PUB-3186, Stanford Linear Accelerator Center, CA (USA) (1983). <https://doi.org/10.2172/5746569>
17. T. Suwada, Multipole analysis of electromagnetic field generated by single-bunch electron beams. *Jpn. J. Appl. Phys.* **40**, 890 (2001). <https://doi.org/10.1143/JJAP.40.890>
18. C. Xu, S. Babel, S. Hoobler et al., Design of an ultra-compact stripline BPM receiver using microTCA for LCLS-II at SLAC, in *Proceedings of 2nd International Beam Instrumentation Conference*, Oxford, UK, 16–19 September 2013
19. C. Kim, J. Hong, H. Kang et al., Stripline beam position monitor for the PAL-XFEL, in *6th International Beam Instrumentation Conference*, Michigan, USA, 20–24 August 2017
20. J.H. Ko, C.H. Shim, I. Nam et al., Two-dimensional tilt control of electron bunch for x-ray free electron laser. *Nucl. Instrum. Meth. A*. **986**, 164726 (2021). <https://doi.org/10.1016/j.nima.2020.164726>
21. H.-S. Kang, H. Yang, G. Kim et al., FEL performance achieved at PAL-XFEL using a three-chicane bunch compression scheme. *J Synchrotron. Radiat.* **26**, 1127–1138 (2019). <https://doi.org/10.1107/S1600577519005861>
22. Based on the data of the MicroTCA-based electronics (<https://www.struck.de/nss11xtcaws.pdf>), the noise level of this electronics is about 4.6 RMS / 32768. If the default reference voltage range is ± 1 V, the noise level would be about 140 μ V RMS. In the actual experiments, after averaging over repeated measurements, the noise level approached to ~ 10 μ V. This final noise level was mainly associated with the RF system

Springer Nature or its licensor (e.g. a society or other partner) holds exclusive rights to this article under a publishing agreement with the author(s) or other rightsholder(s); author self-archiving of the accepted

manuscript version of this article is solely governed by the terms of such publishing agreement and applicable law.